Master of Science Thesis

Quantification and Absorbed Dose Estimation of ^{124}I using microPET

Magnus Hörling

Supervisor: Sven-Erik Strand

Medical Radiation Physics
Clinical Sciences, Lund
Lund University, 2006

ABSTRACT

Small-animal positron emission tomography (PET) has proven to be a promising and useful modality for preclinical pharmacokinetic studies. Thanks to high sensitivity and spatial resolution in the range of a few millimetres, the possibility to perform reliable and accurate quantification and absorbed dose estimates is within reach.

In preclinical radioimmunotherapy (RIT), the slow targeting and clearance kinetics of the tumour targeting antibodies used as radionuclide carriers call for a PET tracer enabling imaging over a period of several days. In this respect, with a half-life of 4.2 days, ^{124}I is more or less an ideal tracer for such studies, also bringing with it well known chemical properties and labelling methods. However, due to complex decay properties, including emission of gammas of energy similar to that of annihilation photons, there are complications of using ^{124}I in PET.

Purpose: The aim of this work was to acquire knowledge of how the properties of ^{124}I affect image quality in small-animal PET. Furthermore, the purpose was to perform an *in vivo* study including quantification, upon which absorbed dose estimates were to be based.

Methods: To begin with, a basic comparison of image quality obtained with ^{124}I and the routinely used positron emitter ^{18}F was performed. This was done using a couple of in-house fabricated phantoms, imaged using a microPET R4 scanner - the PET scanner used throughout this work. Secondly, as a step in the process of deciding how to quantify ^{124}I, the ability of direct quantification of ^{18}F *in vivo* was studied. The quantified activity concentrations were compared to those of biodistribution studies of the imaged mice. Finally, a quantitative pharmacokinetic study of an ^{124}I labelled monoclonal antibody (MAb) was performed in a mouse model, data from which were used for absorbed dose estimates.

Results: An appreciable reduction in spatial resolution and hot-to-cold image contrast was demonstrated in the image quality comparisons of ^{124}I and ^{18}F. The response to different activity concentrations was found to be linear for both ^{124}I and ^{18}F, but with a considerable loss of recovery with ^{124}I. The outcome of the direct quantification of ^{18}F *in vivo* showed variations that did not encourage quantification of ^{124}I solely based on PET image data. Instead, the PET data from the last time point was normalized to corresponding values from a direct assay, done immediately after the last time point PET scan. Good agreement between quantification of activity concentration in blood, based on direct assay of tail vein blood samples and normalized PET data, encouraged the use of this method. The absorbed dose estimates indicated an absorbed dose to tumours of between 3 to 4 Gy, indicating a non-negligible radiotherapeutic effect.

Conclusion: This study indicates that the microPET R4 scanner is capable of reproducing changes in activity distribution of ^{124}I *in vivo*. By normalizing the relative uptake values from the PET images to a direct assay, done immediately after the last time point PET scan, quantification of activity concentration could be done under fairly straightforward conditions. This allowed absorbed dose estimates to be calculated.

TABLE OF CONTENTS

INTRODUCTION

Ever since the pioneering radionuclide treatment of hyperthyroidism and thyroid carcinoma in the early 1940s, different isotopes of radioiodine have had a significant, not to say dominating, role in the field of radionuclide therapy. ^{131}I, for example, emits medium range beta particles, suitable for killing tumour cells growing as small clusters, and is routinely used for post-surgery treatment of thyroid cancer and thyrotoxicosis *(1)*. ^{125}I emits short range conversion and Auger electrons (ranges in the order of nm-µm) and is therefore the isotope of choice when the malignancy grows as single cells. The biogenic amine precursor meta-iodobenzylguanidine (MIBG) labelled with either ^{125}I or ^{131}I has lately been used for treatment of pheochromocytoma and neuroblastoma *(2)*. Further possible clinical applications of radionuclide therapy using ^{125}I have been suggested in the literature *(3)*.

One aspect of vital importance in radionuclide therapy is the ability to administer the radionuclides to the tumour cells in such a way that the uptake, and hence the absorbed dose, in normal tissue is minimized. One strategy used to accomplish this is to deliver the radionuclide to the tumour cells utilizing specific tumour targeting molecules as carriers. The radionuclide is conjugated to a monoclonal antibody (MAb) which specifically targets antigens or receptors that are over-expressed (i.e., compared to the expression in the majority of normal cells) in, or ideally unique to, tumour cells. There are several different classes of tumour associated antigens, of which carcinoembryonic antigen (CEA) and the group of differentiation CD antigens, e.g., CD-20 and CD-22, are important examples bound to the cell membrane. This is, in short, the basic concept of radioimmunotherapy (RIT). There is further advantage in using an antibody as the carrier, in that the MAb in its own often has a cytotoxic effect, resulting in an increased therapeutic effect on the tumour cells. Hence, since it is dependent on both biological factors and radiation effects (namely induced severe DNA damage), RIT is a combination of immunotherapy and radiotherapy.

One benefit of using radioiodine in the context of RIT is that the labelling of biomolecules with iodine is a well known process. This process is in some respects considered easier than labelling with ,e.g., metals, since no chelate (an intermediary molecule) is needed.

Radiolabelled MAbs have successfully been used in lymphoma treatment. In the US, the Food and Drug Administration (FDA) has approved the use of Bexxar, a murine antibody (tositumomab) labelled with ^{131}I, for the treatment of CD20-positive follicular non-Hodgkin's lymphoma *(4)*. So far there has been limited success in the efforts to treat solid tumours using RIT, mainly because of insufficient level of tumour uptake. However, there are many promising improvements under investigation in pre-clinical animal model stages, including optimization of antibody (or antibody fragment) size and binding affinity, regulation of cell surface antigen expression and choice of radionuclide.

Before the evaluation and development of a new radiopharmaceutical or imaging tracer may be taken to a clinical phase, it should be studied in small animal models of disease. In order to perform pre-clinical assessment of the

pharmacokinetics of a radiopharmaceutical, enabling dosimetry and optimization of treatment, the activity concentration in organs and tissues of interest has to be quantified. Currently, the common method of doing this is through necropsy-based biodistribution studies, i.e., measurement of the activity in dissected organs and tissue samples of known weight. Naturally, the need to sacrifice the animal means that one animal only provides data for a single time point, meaning that for each time point of interest a different animal has to be used. In addition to this, in order to gain statistical significance so that comparison of the different time points is meaningful, each time point has to be represented by data from more than one animal. Consequently, this method often requires a large number of animals to be studied and sacrificed. However, thanks to the tremendous development in the field of small animal imaging in the last decade *(5)*, such imaging now seems to offer an alternative way to perform quantitative studies. One advantage of using a non-invasive imaging modality for this purpose is that one single animal provides data for all time points studied. This way, control is gained over the individual animal kinetics and influence of inter-animal differences is evaded. In addition to improved statistics, this method saves animals, labour time and therefore - in the long run - is very cost-efficient.

Thanks to its high sensitivity and spatial resolution, small-animal positron emission tomography[1] (PET) has proven to be a promising and highly useful modality for preclinical pharmacokinetic studies. There are several potential improvements (besides the constant progress in hardware design) that will further strengthen the potential of (quantitative) small-animal PET and broaden the context in which this modality can be used. These improvements include optimization of image reconstruction algorithms and development and implementation of different corrections, e.g., for attenuation, scattered events and positron range, yet to be implemented into these algorithms.

An Iodine Isotope for PET

By definition, the utilization of PET demands a positron emitting radionuclide. Thus, in order to be able to study the behaviour and pharmacokinetics of an iodine-labelled molecule using PET, a positron emitting iodine isotope is needed. ^{124}I is such an emitter, making these kinds of studies possible. The half-life of ^{124}I is approximately 100 h, or 4.2 days. In this respect, it is more or less an ideal tracer for the study of biomolecules, since it enables imaging over several days. This is often needed, due to the relatively slow targeting and clearance kinetics of biomolecules (including antibodies), not least in order to obtain enough pharmacokinetic data to allow reliable dose estimates.

A shorter half-life, in the order of hours (as in the case of ^{18}F, widely used for the PET tracer fluorodeoxyglucose), would not allow long-time imaging without impractically and unjustified high amounts of activity being administered. Too long a half-life, on the other hand, may result in an excessive absorbed radiation dose, when the purpose is solely imaging (i.e., non therapeutic). In addition to this, the longer the half-life, the more effort and care has to be put into radiation safety, in terms of storage and handling of residuals and waste.

[1] For the basic physics, principles and terminology of PET, the reader is referred to introductory literature, such as *(6)*.

Another benefit of the relatively long half-life of ^{124}I is that it allows the use of activity produced by a remote radionuclide production facility, thus eliminating the demand for an on-site cyclotron.

However, due to its decay properties, there are some drawbacks and complications of using ^{124}I in PET, as discussed below.

Challenging Decay Properties

^{124}I has a complex decay scheme (Figure 1). In addition to positrons, it also emits single gamma photons in a great number of different energies (more than 90 possible transitions). It is therefore often referred to as a non-pure or, in more popular terms, 'dirty' positron emitter. The two most abundant gamma photons have energies of 603 keV and 723 keV (63% and 10% abundance, respectively). These energies are unfortunate from a PET point of view, since the photons are accepted by the discriminator of the annihilation photon energy window, at least after Compton scatter, but possibly even in primary form, depending on the upper threshold of the energy window. This results in an increase of the accidental coincidence counts, something that may have an impact on image contrast.

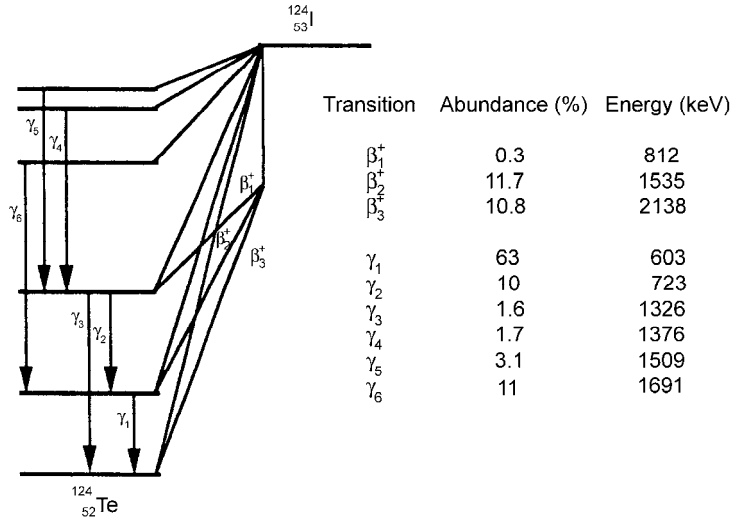

Transition	Abundance (%)	Energy (keV)
β_1^+	0.3	812
β_2^+	11.7	1535
β_3^+	10.8	2138
γ_1	63	603
γ_2	10	723
γ_3	1.6	1326
γ_4	1.7	1376
γ_5	3.1	1509
γ_6	11	1691

FIGURE 1. Simplified decay scheme of ^{124}I. Indicated are three different positron transitions and the six most abundant gamma transistions.

Of at least four different positron emissions possible, only two have significant probability. The total abundance of these two is rather low, only 23%, compared to the 97% positron yield of ^{18}F. At endpoint energies of 1535 keV and 2138 keV, respectively, these positrons are also of higher energy than those emitted by ^{18}F (634 keV). In terms of range (root mean square (rms), in water), this means approximately[2] 0.8 mm and 1.3 mm, in other words significantly longer than the 0.2 mm of the positrons from ^{18}F. This increase in range, resulting in an increase in the perpendicular distance from the site of emission to the line of response (LOR, i.e., the line defined by the annihilation photons), causes a degradation of the spatial resolution, leading to an unfavourable effect on quantification.

[2] Approximations based on data from *(7)*.

In addition to this, approximately 50% of the positrons are emitted in cascade with a 603 keV gamma photon (referred to as a *prompt gamma*). This causes another complication, since 'true' events derived from coincident detection of a prompt gamma and one of the annihilation photons will occur. Events like these are here referred to as *prompt gamma coincidences*. Because the direction of the prompt gammas (no matter scattered or not) have no correlation with that of the annihilation photons, the recorded lines of response from such events provides no information about the actual activity distribution within the studied object.

Comment on the Partial Volume Effect

Just like all imaging modalities used in nuclear medicine, PET systems have limited spatial resolution. This means that an infinitely small source of radiation will be detected as an object of finite size. As a result of this 'smearing' in the reconstructed PET image, the activity concentration of small structures and organs, comparable in size to the spatial resolution of the scanner, will appear lower than the actual value. This phenomenon is commonly referred to as the *partial volume effect (8)*.

Purpose of This Work

The aim of this study was to acquire knowledge and understanding of how the properties of ^{124}I affect image quality in small-animal PET. Furthermore, the purpose was to study the possibility to perform quantification of ^{124}I for pharmacokinetic assessment and dosimetry in pre-clinical RIT research.

In recent years, imaging with ^{124}I has been used to visualize, localize and demonstrate uptake of monoclonal antibodies (or engineered fragments) in tumour xenografts in mice, using microPET *(9)* and clinical PET/CT *(10)* scanners. However, to the author's knowledge, this is the first reported attempt of absolute quantification and absorbed dose estimates of ^{124}I in mice using a dedicated small-animal PET scanner.

The work described took the form of three main parts. To begin with, a basic comparison between ^{124}I and the routinely used positron emitter ^{18}F was done, in terms of spatial resolution, shape and amplitude of image background and hot-to-cold contrast. Furthermore, the ability of the scanner to linearly reproduce different activity concentrations, and to what extent the actual activity concentrations were recovered was studied.

Secondly, as a step in the process of deciding how to quantify ^{124}I, the ability of direct quantification of ^{18}F *in vivo* using only the PET image data was studied. The quantified activity concentrations were compared to those of biodistribution studies of the imaged mice.

Finally, a quantitative pharmacokinetic study of an ^{124}I labelled MAb was performed in a mouse model. The data were used for calculation of absorbed dose estimates.

MATERIALS & METHODS

PET Scanner

The PET system used in this work was the microPET R4 (Concorde Microsystems Inc., Knoxville, TN) installed at City of Hope National Medical Center, Duarte, CA (Figure 2). The R4 is a commercially available version of the original prototype small-animal PET scanner, designed and developed at the Crump Institute for Molecular Imaging, UCLA *(11)*. It is dedicated to the scanning of small rodents, mainly mice and rats. The scanner does not use any kind of inter-plane septa and therefore operates exclusively in 3D mode.

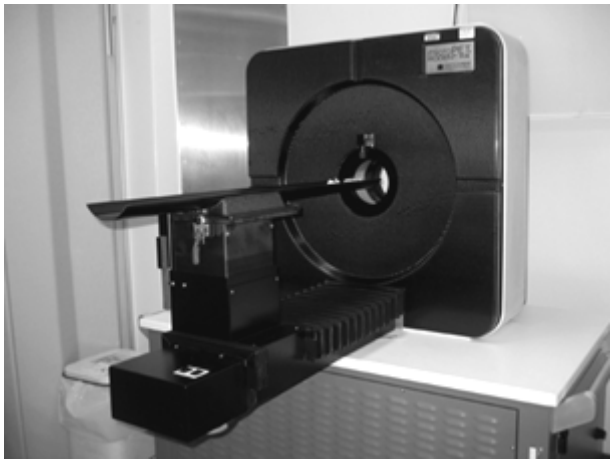

FIGURE 2. The microPET R4 scanner installed at City of Hope National Medical Center.

The scanner consists of four detector rings with a diameter of 148 mm. The resulting animal port is 120 mm in diameter. Each ring consists of 24 detector blocks made out of the scintillating crystal material lutetium oxyorthosilicate (LSO). The blocks measure 19×19×10 mm^3 and are cut into 8×8 arrays of 2.1×2.1 mm^2 elements. For each block the 64 crystal elements are optically coupled to a position-sensitive photomultiplier tube (PS-PMT, Hamamatsu Photonics K.K., Japan), on the back of which is situated an electronic read-out board.

The electronic field of view (FOV) is 78 mm in the axial direction, while in the transaxial direction it is limited to 100 mm. Scatter contribution from activity outside of the FOV is reduced by a lead shield around each side of the animal port.

For placement and positioning of animals and phantoms, the scanner is equipped with a computer controlled carbon fibre (for minimized effect of scatter and attenuation) bed. Positioning is aided by a laser system located over the animal port at the front of the scanner.

For all studies within this work, the energy window setting was 350-750 keV. The system automatically corrects for dead-time. The same applies to correction for positron branching ratio, given that appropriate isotope settings are chosen for the acquisition. In these studies correction for decay during acquisitions was chosen.

Random coincidences are corrected for using the delayed window subtraction method. The coincidence time window was set to 6 ns. All data were acquired in list mode.

The performance of the microPET R4 has been thoroughly evaluated and described in the literature *(12), (13)*.

Radionuclides

^{18}F was used in the form of radiopharmaceutical grade ^{18}F labelled fluoro-deoxyglucose (^{18}F-FDG) produced by Cardinal Health (Colton, CA) and delivered in an activity concentration of approximately 370 MBq/ml.

Cyclotron produced ^{124}I *(14)* was bought and delivered from IBA Molecular/Eastern Isotopes (Sterling, VA) in an activity concentration of about 3 MBq/µl. The radiochemical purity was specified as >95%, whereas the radionuclidic purity was >99,9%.

Antibody and Labelling

The MAb used was the anti-CEA (carcinoembryonic antigen) chimeric T84.66 (cT84.66) *(15)* labelled with ^{124}I using the Iodogen method *(16), (17)*. The labelling efficiency was about 70%. After column purification this value increased to 98% or better, meaning that the level of free iodine was less then 2%.

Normalization Scan

A normalization file was acquired by scanning a 50 ml tube of 28 mm inner diameter filled with approximately 89 MBq of ^{18}F-FDG at the start of the scan. Data were collected for 5 h. This information is used by the system to correct for the fact that the different detectors have slightly different efficiency characteristics (detector non-uniformity). This file was then used in conjunction with all image reconstruction.

Image Reconstruction

All histogramming and reconstruction was done in the Visual C++ based user interface called microPET Manager (also used to control the actual data acquisition). The list mode data were rebinned and histogrammed into 3D sinograms using a span of 3 and a ring difference of 31 (default settings). These settings affect how much of the full 3D data set (the list mode raw data) is used when the data are binned (and rebinned) into sinograms. Simply put, ring difference specifies how many crystal rings away from a given ring the rebinning algorithm should look for a coincidence event. Span specifies how many adjacent lines of response (LOR) should be grouped together, representing the same axial angel.

For the phantom studies two different kinds of reconstruction algorithms were used. The first was a standard 2D ordered subsets expectation maximization (OSEM) algorithm *(18)*, in this case incorporating Fourier rebinning (FORE, *(19)*) and 4 iterations of 16 subsets. The second algorithm was a combination of two; 3D OSEM and a maximum *a posteriori* (MAP) algorithm *(20)*. This combination was used in a setup where the reconstruction started by making two OSEM iterations of 12 subsets, thereafter switching to MAP, of which 18 iterations were

made. The smoothing value (β) associated with MAP was set to 0.01 and the optional uniform resolution setting was selected. Below, this combined algorithm is referred to simply as MAP. Basic comparisons were then done between the results obtained with the OSEM reconstruction method and the MAP ditto.

Both types of reconstruction resulted in an image matrix of 128×128×63 voxels. Each voxel measured 0.85 mm in the radial and tangential directions. With a slice thickness of 1.2 mm this gave a voxel volume of about 0.87 mm^3.

The *in vivo* studies were all reconstructed using the MAP algorithm. All reconstructions were done without applying any corrections for attenuation and/or Compton scatter[3].

Image Analysis

Image viewing and analysis was done in the IDL-based (Interactive Data Language, Research Systems Inc. Boulder, CO) analysis software ASIPro, provided by the manufacturer of the scanner. This program contains a profile tool and a tool for creating volumes of interest (VOI).

Phantom Studies

Four different kinds of phantom studies were done. The purpose and experimental procedures of each of those are described below.

All activities were measured using a Capintec CRC-7 activity meter (Capintec Inc., Ramsey, NJ), calibrated using a NIST certified ^{137}Cs standard source and set to appropriate settings. Stock solutions of known volume and activity were used to prepare solutions of lower activity concentration. This was done by adding a known weight of the stock solution to a measured volume of water.

Spatial Resolution

In order to investigate if the spatial resolution obtainable with this system is comparable to the values that the manufacturer and other investigators report, a simple spatial resolution phantom was constructed (Figure 3). More importantly, this also was done to get a direct comparison of the spatial resolution for ^{18}F and ^{124}I.

The phantom consisted of a water filled 40 mm diameter plastic bottle containing three capillary tubes of approximately 1 mm inner diameter. These were filled with activity solution, hence acting as line-sources. The capillary tubes were held in place by two pieces of Styrofoam and positioned, fairly aligned, at the centre, 8mm and 16 mm off-centre respectively, the two latter at an angle of 90º relative to each other. Two phantoms were made – one for ^{18}F and one for ^{124}I.

[3] See RESULTS & DISCUSSION for comment.

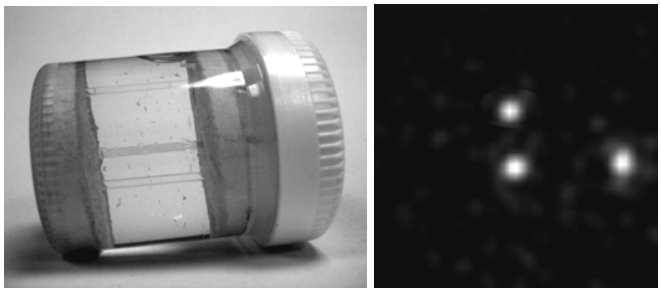

FIGURE 3. The spatial resolution phantom (left) with the three capillary tubes visible, and a transaxial slice of the phantom with ^{124}I (right) reconstructed using the MAP algorithm.

After positioning the phantom on the scanners bed, with the length of the capillary tubes running in the scanner's axial direction and the centre tube approximately in the centre of the FOV, a 30 min scan was performed. At the start of the scan the activity concentration in the capillary tubes was about 185 kBq/ml for the ^{18}F phantom and about 370 kBq/ml in the case of ^{124}I.

For each of the three different positions FWHM values were generated for ten adjacent slices using the profile tool's automated Gaussian fit. The mean of the FWHM values in each position were then plotted. An over-all mean FWHM was also calculated using values from all three positions. The ten profiles of the central line-source were exported to a spreadsheet (Excel, Microsoft Inc., Redmond, WA) where they were summed. This data was then used to fit Gaussian functions in IDL, in their turn used to see how well such a shape represents the profiles of the two isotopes and if the FWHM values of these fits were agreeable with the calculated mean values mentioned above.

Calibration Factors

In order to convert the average voxel value (AVV) within a VOI to a corresponding activity concentration (AC), a conversion factor is needed. This factor is called the calibration factor (CF) and should be measured for every separate isotope of which quantification is of interest. The relationship between activity concentration, AVV and the calibration factor is shown in the equation below.

$$AC\left[Bq\,ml^{-1}\right] = AVV\left[ml^{-1}\,s^{-1}\right] \cdot CF\left[Bq\,s\right]$$

For each of the two isotopes a 20 ml vial (26 mm in diameter and 60 mm in length) filled with a known amount of activity was scanned for 30 minutes. In the case of ^{18}F the activity concentration at the start of the scan was about 377 kBq/ml. The corresponding value for the ^{124}I scan was approximately 74 kBq/ml. A cylindrical VOI encompassing 25-30 transaxial slices of the vial was drawn in the reconstructed image data. The calibration factor for each case was then obtained by dividing the known activity concentration by the AVV.

Activity Concentration Linearity and Recovery

Instead of assuming the system to have a linear activity concentration response *(21)*, it was decided to investigate if this seems to be the case for the microPET R4. A phantom (from now on referred to as the *linearity phantom*) was made out of a plexiglass rod (63 mm in length and 35 mm in diameter), approximately the size of a mouse (Figure 4A). Four holes (6.8 mm in diameter) were drilled, equally distanced at 10 mm from the centre of the rod. In the holes 1 ml syringes (approximately 5 mm inner diameter) filled with solution of different activity concentration were positioned. This would demonstrate the ability to recover the activity concentration in an object of fairly small diameter, and whether or not the response would differ for ^{18}F and ^{124}I, given their different decay and positron properties.

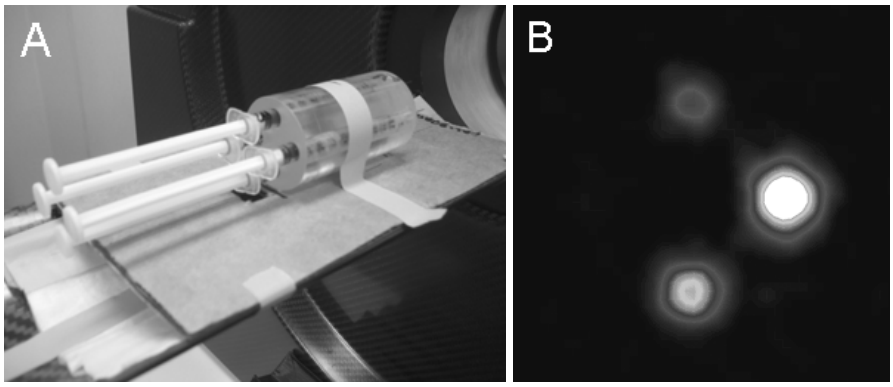

FIGURE 4. (A) The linearity phantom positioned in the scanner. (B) A transaxial slice of four different activity concentrations of ^{124}I (MAP reconstruction). In order for the forth syringe to appear, the image threshold had to be set significantly lower than was the case in this image.

The activity concentrations were chosen to roughly represent the range of activity concentrations one can expect in the blood, organs or tissue in an *in vivo* study of a mouse injected with a positron emitting radiopharmaceutical. The phantom was placed on the bed of the scanner, with the centre approximately in the centre of the FOV. This setup was scanned for 30 minutes, with separate scans for ^{18}F and ^{124}I.

In the reconstructed images (an example of which is found in Figure 4B) a VOI was created for each syringe, consisting of the 4 hottest adjacent voxels in each of 25-40 slices. The average voxel value within each VOI was then multiplied with the appropriate calibration factor and the resulting calculated activity concentrations were plotted versus the actual measured values. The recovery fractions, i.e., the ratio between the activity concentrations calculated based on the PET image data and the actual values measured with the activity meter, were also calculated.

Image Background and Contrast

In order to compare the level and shape of the background with ^{18}F and ^{124}I, a phantom was constructed (Figure 5A) from a 20 ml vial of the same kind as the calibration phantoms described above. By including an insert consisting of a 0.6 ml tube filled with water, half of the phantom could also be used to compare the image contrast between a hot and a cold region in the two cases. Below this

phantom is referred to as the *inhomogeneity phantom*. In both the case of ^{18}F and ^{124}I the activity concentration was approximately 90 kBq/ml at the time of scan.

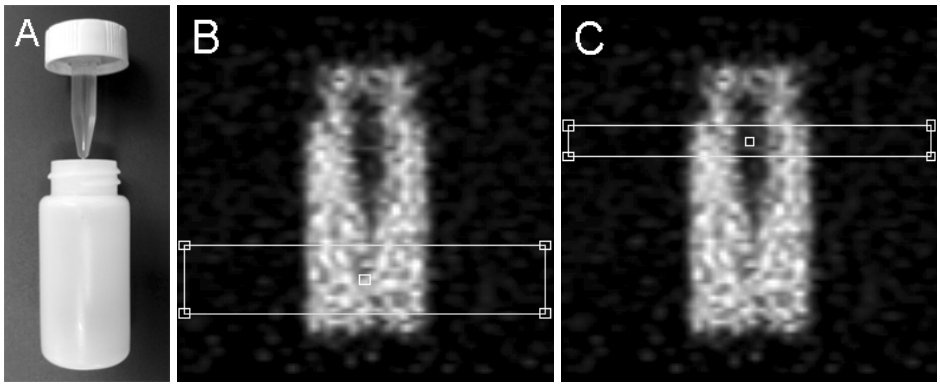

FIGURE 5. The inhomogeneity phantom (A) and coronal slices of the phantom with the profile window positioned over the homogeneous part (B) and over the part including the water filled insert (C). The images shown here are from the scan of ^{124}I, reconstructed with the MAP algorithm.

Profile windows were placed in the coronal slice corresponding to the middle of the phantom in the reconstructed images. These windows, representing the region from which the profile data is taken, spanned over most part of the radial width of the FOV. For the inhomogeneous part of the phantom (i.e., the part with the cold insert) the window included about 6 transaxial slices (Figure 5B), from which a mean profile was taken, whereas for the homogeneous part a region about 15 slices wide could be used (Figure 5C). The resulting profiles were normalized and plotted in Excel for comparison.

Animal Studies

The animals used were 7-8 weeks old female athymic nude mice injected subcutaneously in the right flank region with approximately $1.5 \cdot 10^6$ LS174T human colon carcinoma cells. At the start of the experiments the tumours had grown for about 10 days.

Studies of two groups of mice were done. The first group (fasted for about 12 h before the experiment) was injected with ^{18}F-FDG and the second with the ^{124}I labelled MAb. After tail vein injection, scans were done at different time points post injection (p.i.). In all cases the injected volume was about 0.2 ml.

During the scans the mice were anesthetized using isoflurane (IsoFlo, Abbot Animal Health, Chicago, IL) and immobilized in supine position on a cardboard platform, with the long axis of the mouse parallel to the axial direction of the scanner.

The injected activities were measured with the same activity meter that was used to measure the solutions used in the phantom studies. This was also the activity meter to which the well counter, used to count the dissected organs and tumours (see below), was calibrated.

^{18}F-FDG Study

Study Design

The purpose of the *in vivo* ^{18}F-FDG study was to see how the quantification of the activity concentration based on the PET images compared to the quantification based on well counter activity counting of the corresponding dissected and weighed organs. This was done for two different time points, one close to the injection and one at a time of considerable uptake in tumour and organs.

Two mice were sacrificed 5 minutes post injection of 1.4 MBq and 2.0 MBq respectively and thereafter scanned for 10 minutes, representing a 5 minute time point. The reason why these mice were imaged *post mortem* is that the uptake of ^{18}F-FDG is rapid and therefore the distribution changes substantially at such an early stage. These processes were considered to stop when the animals were sacrificed, although a certain degree of diffusion could possibly occur, most likely of minor significance in this context though. Thereby the *post mortem* acquisition of PET data and the assay of the studied organs and tumour in the well counter represent the same situation of activity distribution.

Two more mice, both injected with 2.1 MBq, were scanned *in vivo* for 65 minutes from the time of injection. Data from the 10 last minutes (55-65 minutes p.i.), representing a 1 h time point, were used for the analysis.

Activity Concentration Quantification

When the scanning of a mouse was finished it was dissected and the liver, heart, kidneys and tumour were weighed and thereafter counted in a combined NaI(Tl) well counter and automated sample changer (Wizard 3", Wallac Oy, Turku, Finland). By dividing the measured activity by the corresponding weight, the

activity concentration in the studied tissue was obtained. From now on this procedure is referred to as the *direct assay*.

In the reconstructed images a VOI was created for each of the regions to be studied. All VOI definitions were made in the transaxial view. For the tumours the VOI consisted of the four voxels with the highest signal. Such a small region was chosen in order to minimize under-estimation of the activity concentration due to the partial volume effect. In the case of the kidneys and the heart, larger regions were used, encompassing voxels down to about 50-70 % of the maximum voxel value within the organ. For the liver, not clearly distinguishable in any of the studies, a VOI was drawn over what was assumed to be the middle and the right lobe of the liver, in about 3 slices between the heart and the stomach region. The averaged voxel value of a VOI was multiplied with the calibration factor to yield the activity concentration, which then was compared to the corresponding direct assay value.

^{124}I-cT84.66 Study

Study Design

Two mice were injected with ^{124}I labelled anti-CEA cT84.66 MAb, about 1.7 MBq and 1.6 MBq respectively, and scanned at 7 time points through 8 days. The time points were 1 h, 4 h, 21 h, 45 h, 69 h, 141 h and finally 165 h (166 h for the second mouse) p.i. At the three first time points, the mice were scanned for 20 minutes, at the fourth and fifth for 30 minutes and at the two last time points for 40 minutes. Just before and just after each scan a 10 µl tail vein blood sample was taken for direct assay of the blood activity concentration. The mean value of the before and after samples was used for comparison with PET data from the corresponding time point. After completion of the last scan, the mice were sacrificed and livers and tumours were dissected for direct assay. A coronal view of mouse #1 at three different time points is shown in Figure 6.

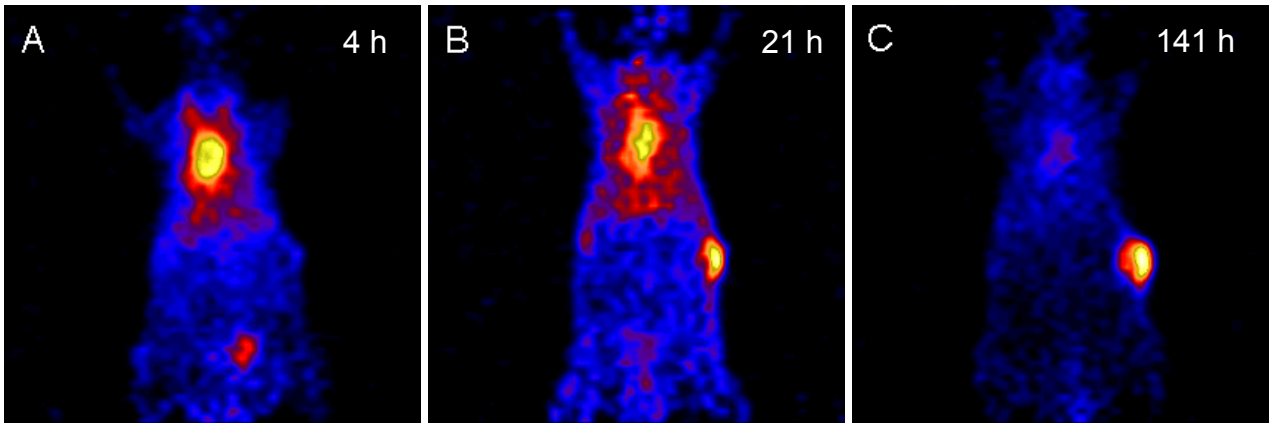

FIGURE 6. Coronal view of a ventral segment of mouse #1, at 4h (A), 21h (B) and 141 h (C) p.i. In (A) the image is dominated by activity in blood pool and blood rich regions, mainly heart. In (B) the situation has changed in that the liver region is slightly more evident and the uptake in the tumour (located in the animal's right flank) has reached a level of clear visualization. At 141 h p.i. (C) a significant uptake, compared to surrounding tissue, can be seen in the tumour. Some residual activity is still visible in the heart region.

Activity Concentration Quantification

Quantification of the activity concentrations based on the PET images of the different time points was done for tumour, liver and blood. For tumour and liver, the VOI definition was done in the same way as in the ^{18}F-FDG study, except that bigger tumours allowed for a few more voxels to be included in the tumour VOI (4-8 voxels). To get blood values a VOI encompassing the four hottest adjacent voxels in the heart region was created (corresponding to blood in the left ventricle). Due to uncertainties in animal position and possible organ movement, each VOI was defined separately for each time point. A VOI was also defined for the whole body. This encompassed all voxels in the entire FOV and thereby gave an AVV proportional to the total activity in the animal at each time point (all counts within the FOV was assumed to originate from the studied animal).

The variations seen in the outcome of the ^{18}F-FDG study led to the choice of a slightly different approach for the quantification of ^{124}I, on which the absorbed dose estimates were to be based. Instead of using the calibration factor, the AVV for the last time point of each studied region was normalized to the corresponding direct assay value (except whole body, for which the first time point was normalized to the known injected activity after one hour of decay). This method has been used in other microPET contexts by investigators such as Bading et al. *(22)*. The earlier time point AVVs were then multiplied with the normalization factor, i.e., the ratio of the direct assay value and the last time point AVV. This method was encouraged by the good agreement between the direct assay blood curve and ditto PET data normalized this way. Thus, the PET data was used to get the *shape* of the uptake curves, while the *amplitude* was given by normalization to the direct assay. The whole body data were normalized in such a way that the AVV for the 1 h time point represented the injected activity after 1 h of decay (it was assumed that no activity had left the animal after 1 h).

Calculation of Absorbed Dose Estimates

For visualization and comparison of the uptake, clearance and retention of the labelled antibody, time-activity curves (TAC) showing the decay-corrected data were plotted in terms of percent injected activity per gram tissue (% IA / g). The blood weight was estimated as 7 % of the total body weight *(23)*. For the dosimetry, all data used were in non decay-corrected form, since what is of interest for this purpose is the actual remaining activity content at a given time.

Estimation of mean absorbed doses was done using the MIRD formalism for internal absorbed dose calculations *(24)*. The mean absorbed dose ($\overline{D}$) is given by

$$\overline{D} = \tilde{A} \cdot S = A_0 \cdot \tau \cdot S \quad \rightarrow \quad \frac{\overline{D}}{A_0} = \tau \cdot S$$

where $\tilde{A}$ is the cumulated activity and S represents the mean absorbed dose per unit cumulated activity from a given source volume to a given target volume. As shown above, the mean absorbed dose per unit administrated activity ($\overline{D} / A_0$) can be calculated by introducing the so called residence time τ (the cumulated activity per unit administrated activity).

Using the ADAPT II software *(25)* bi-exponentials functions on the form $A_1 e^{-k_1 t} + A_2 e^{-k_2 t}$ were fitted to the (non decay-corrected) time-activity data points. The following integration

$$\tilde{A} = \int_0^\infty A_1 e^{-k_1 t} + A_2 e^{-k_2 t} dt = A_1 / k_1 + A_2 / k_2$$

resulted in the estimated cumulated activity (the area under the fitted curve), which after division by the injected activity (IA) gave the corresponding residence time value.

^{124}I S values for liver and whole body were obtained by Monte Carlo simulation in a digital mouse phantom *(26)*. The phantom was scaled to represent a 9 cm long mouse (tip of nose to root of tail), an approximate average length for mice of the kind and age used. This phantom did not include any tumour. Since both tumours were close to spherical in shape, approximate tumour S values could be obtained by using the sphere model in the OLINDA software *(27)*. Resulting S values for five spheres of mass ranging from 0.01-2.00 g were plotted in Excel. By fitting a power function to these data, approximate S values could be calculated for the masses of the two studied tumours.

RESULTS & DISCUSSION

Phantom Studies

Spatial Resolution

The mean of the FWHM values for ten adjacent profiles obtained from ASIPro is plotted for each of the line-source positions in Figure 7. With ^{18}F the FWHM seems to be in the range of 1.8-2.2 mm, without any major differences between the two reconstruction methods, although the margins of error (the standard deviation in FWHM for each set of ten profiles) are smaller for MAP. In the case of ^{124}I the variation of the FWHM in the different positions in the FOV is more pronounced, especially with the OSEM reconstruction with values from about 2.3 mm to 3.0 mm. The MAP algorithm seems to do a slightly better work in keeping the spatial resolution more uniform over the FOV.

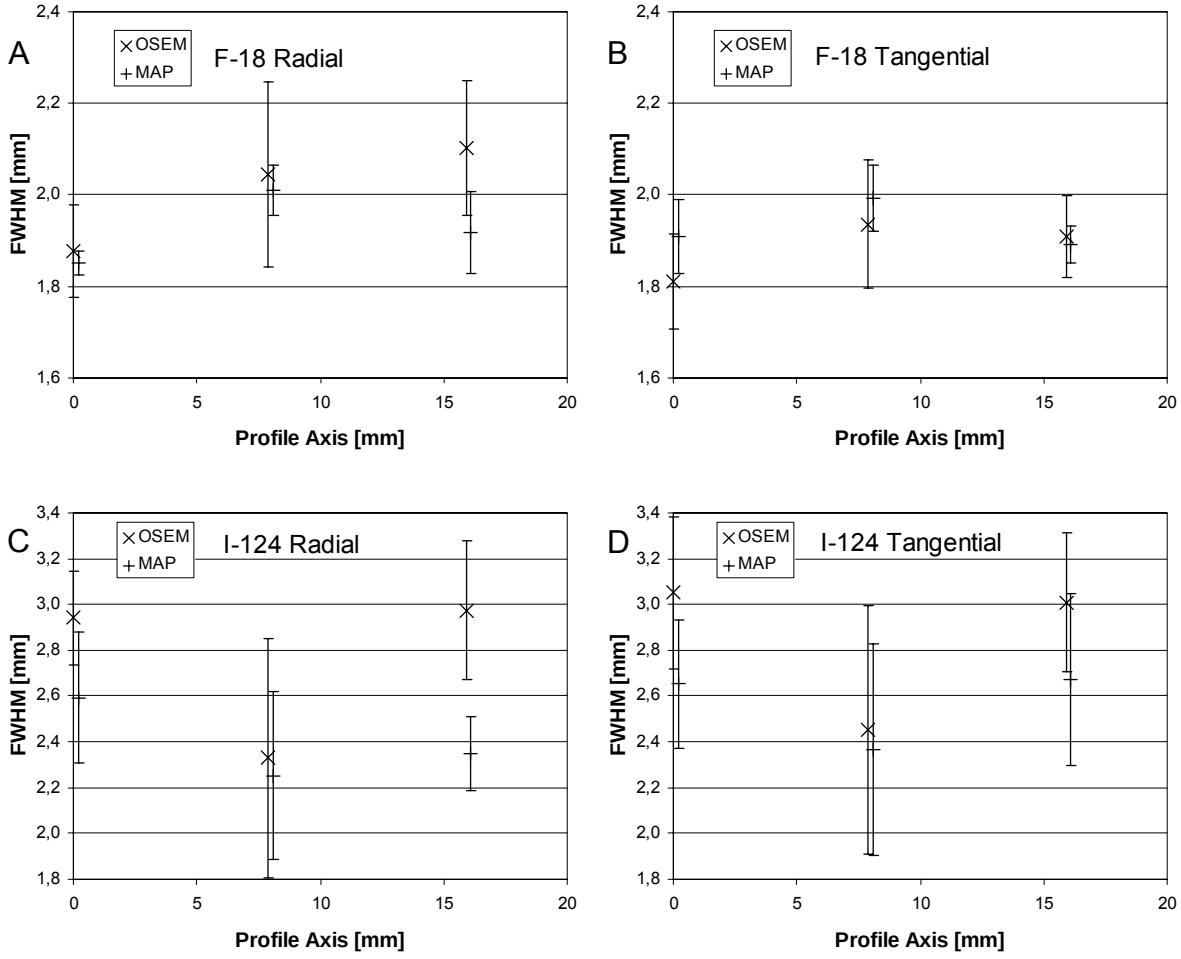

FIGURE 7. Results of the spatial resolution phantom study. Plotted are the mean FWHM values of ten profiles from adjacent image slices for the radial (horizontally across the bore of the scanner) and tangential (vertically across the bore of the scanner) directions. The mean FWHM for each combination of isotope and reconstruction method, without any distinction between position and direction in the FOV, can be found in Table 1.

Given the variations in spatial resolution seen in Figure 7, it seems the mean of the obtained values in the different positions could provide a reasonable representation of the general spatial resolution that can be expected within a radius of about 15 mm from the centre of the FOV. This part of the FOV corresponds well to what is used when scanning a mouse, provided that the animal is aligned and centred prior to the scan. The mean values for each combination of isotope and reconstruction are found in Table 1.

TABLE 1
Mean FWHM values

^{18}F		^{124}I	
Reconstruction	FWHM (mm)	Reconstruction	FWHM (mm)
OSEM	1.9 ± 0.2	OSEM	2.8 ± 0.5
MAP	1.9 ± 0.1	MAP	2.5 ± 0.5

The reduction in spatial resolution seen with ^{124}I will not only have a negative effect on the ability to resolve small anatomic structures, but will also affect direct quantification in terms of a lower recovery when an object has a size close or comparable to the FWHM. In other words; the partial volume effect will be more pronounced.

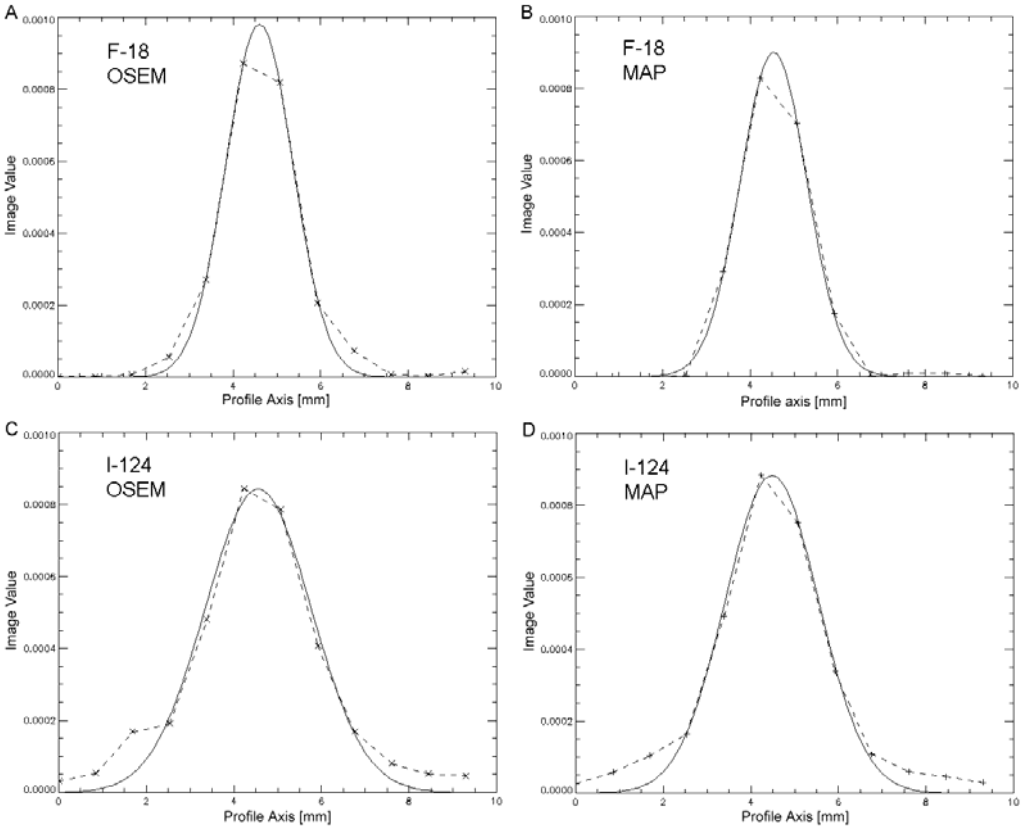

FIGURE 8. Mean profiles of ten adjacent image slices of the line source positioned approximately in the centre of the FOV. The solid lines represent Gaussians fitted using IDL. For ^{18}F the FWHM is 1.8 mm both in the case of OSEM (A) and MAP (B) reconstruction. For ^{124}I the FWHM is 2.9 mm with OSEM (C) and 2.5 mm with MAP (D).

The FWHM values in Table 1 are in fair agreement with those of the Gaussian fits found in Figure 8. In the case of ^{18}F there is a good agreement between the fitted Gaussians and the data points, especially in the case of the MAP reconstruction. Hence, this demonstrates that a Gaussian function is a good representation of the shape of these profiles.

The relatively poor agreement between the actual measured data and the fit of the flanks of the ^{124}I profiles is probably a result of the contribution from the prompt gamma background, causing the less Gaussian shape of these profiles, as compared to those of ^{18}F. The "tails" of the ^{124}I response function will have negative impact on contrast.

To the author's knowledge only one investigator has reported FWHM values for the microPET R4 scanner, then measured using ^{22}Na ($E_{\beta,max}$=0.55 MeV). Unfortunately no such data have been found published for ^{124}I. Knoess et al. *(12)* measured 1.7 mm with a 1-mm-diameter ^{22}Na point source using a filtered back projection algorithm, while Concorde, the manufacturer of the scanner, state a FWHM $\leq$ 1.8 mm, not specifying what isotope was used. These values make the spatial resolution results in this work seem very reasonable, especially when the fairly simple conditions under which the measurements were done are considered.

Calibration Factors

In order to perform direct quantification, i.e., quantification based solely on the PET image data, a calibration factor is needed. Therefore, a phantom study was done to obtain this factor for the two different isotopes used in this work; ^{18}F and ^{124}I. The resulting calibration factors for each isotope and reconstruction method, as used in the linearity experiment and the ^{18}F-FDG study, are found in Table 2.

TABLE 2
Calibration Factors

^{18}F		^{124}I	
Reconstruction	CF (kBq s × 10^3)	Reconstruction	CF (kBq s × 10^3)
OSEM	22.5	OSEM	27.5
MAP	23.2	MAP	27.9

As can be seen, the calibration factors are slightly larger for ^{124}I than for ^{18}F. Put in other words, for a given activity concentration, the average voxel value is somewhat smaller when imaging ^{124}I, compared to imaging of ^{18}F. Thus, it seems the sensitivity, or counting efficiency, of the system is lower for a non-pure positron emitter such as ^{124}I, than for ^{18}F.

Activity Concentration Linearity and Recovery

A linear system response within a wide range of activity concentration levels is a key feature in order to perform meaningful and interpretable quantitative work. Whether or not this can be stated to be the case for the microPET R4 was investigated by scanning the linearity phantom. The resulting calculated activity concentration values (AVV·CF), as well as the well-counter measurements of the used aliquots are found in Table 3. Also presented in the table are the

corresponding recovery fractions, expressed as percentage of the measured activity concentration.

TABLE 3
Measured and calculated activity concentrations (AC) and the corresponding recovery percentages

^{18}F

	OSEM		MAP	
Measured AC (kBq/ml)	Calculated AC (kBq/ml)	Recovery (%)	Calculated AC (kBq/ml)	Recovery (%)
880.6	678.5	77	874.0	99
444.0	355.0	80	430.5	97
207.2	153.3	74	189.5	91
14.8	11.4	77	13.6	92

^{124}I

	OSEM		MAP	
Measured AC (kBq/ml)	Calculated AC (kBq/ml)	Recovery (%)	Calculated AC (kBq/ml)	Recovery (%)
788.1	403.8	51	486.7	62
370.0	205.7	56	232.6	63
151.7	84.6	56	97.4	64
14.8	8.7	59	9.9	67

The results are plotted, together with linear fits, in Figure 9. The response appears to be linear in all cases. With the MAP reconstruction the recovery for ^{18}F is very encouraging, with an average recovery fraction of about 95% for the four different activity concentrations. With OSEM there is a drop in recovery of roughly 20%. Apparently the difference in recovery between the two reconstruction methods is more appreciable than one would suggest, solely based on the quite subtle difference in spatial resolution between the two reconstruction methods seen with ^{18}F.

What is most noticeable when the results for the two isotopes are compared is the apparent loss in recovery with ^{124}I. The MAP reconstruction performs slightly better in this regard, but there is still an almost 40% reduction in the achieved recovery when compared to ^{18}F. This confirms what can be expected from the apparent increase in measured FWHM in comparison to ^{18}F and knowledge of the partial volume effect. The diameter of the syringes used in the linearity phantom (5 mm) is just about two times the FWHM value found for ^{124}I with MAP (2.5 mm, see Table 1). According to simulations done by Cherry and Dahlbom *(6)* the resulting recovery for an object twice the size of the FWHM is somewhere between 60-90% in the very peak of the response function. This considered, combined with the fact that the calculated FWHM values in this study are fairly approximate, the approximately 40% loss in recovery found here does not seem any surprising, but instead rather reasonable.

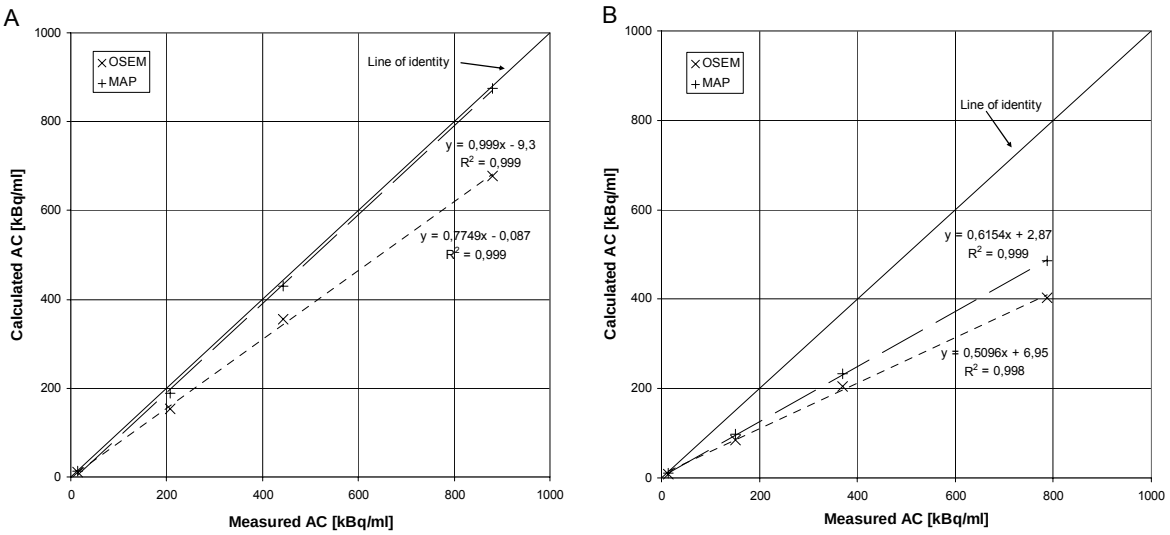

FIGURE 9. Activity concentration response for ^{18}F (A) and ^{124}I (B) using the two different reconstruction methods. The dashed lines represent least square linear fits.

Image Background and Contrast

The resulting normalized profiles from the scans of the inhomogeneity phantom are shown in Figure 10. As seen there is an obvious difference in shape and level of the backround of ^{18}F and ^{124}I. The ^{124}I profiles demonstrate a higher level of background compared to those of ^{18}F, and whereas the amplitude in the case of ^{18}F decreases towards the edges of the FOV the level seems to be almost constant across the entire FOV in the case of ^{124}I. This demonstrates that the prompt gamma coincidences (i.e., events originating from coincident detection of either an annihilation photon and a prompt gamma, or possibly two prompt gammas) are spatially random in nature. The ^{18}F background on the other hand is dominated by scattered events, of which the occurrence decreases with increased distance from the activity source. Of course the scatter component is present in the background from ^{124}I as well, but the sloping shape seems to get drowned in the noise of the prompt gamma coincidences.

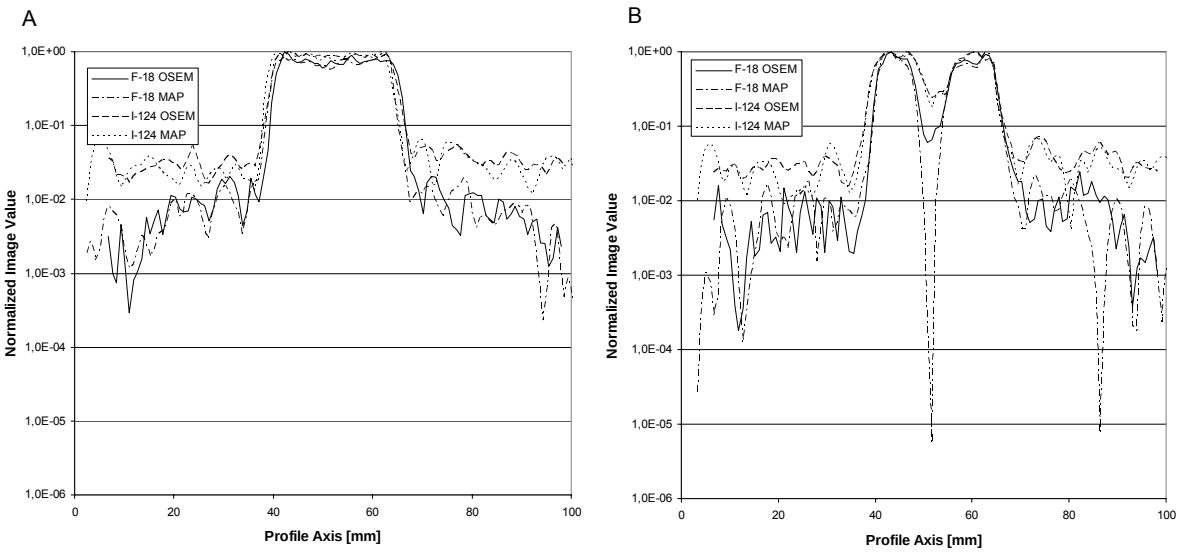

Figure 10. Normalized profiles of the inhomogeneity phantom demonstrating how the background of ^{124}I differs in shape and level from that of ^{18}F (A) and the difference in hot-to-cold image contrast (B). Note log scale on the vertical axis.

In Figure 10 B it can be seen that the hot-to-cold contrast is lower in the case of ^{124}I than with ^{18}F. In the latter case the signal in the cold region is caused mainly by scattered events from the surrounding activity, whereas the corresponding signal in the case of ^{124}I consists not only of scattered events but also of a contribution from the more or less constant background, caused by the prompt gammas. The limited spatial resolution, causing a broadening of the edges of the hot surrounding, also contributes to the signal in the cold region, more so in the case of ^{124}I than ^{18}F because of the longer average positron range.

Regarding the two methods of reconstruction, no evident difference in performance can be seen from these profiles. Possibly with MAP there is a slightly larger variation in the background level of ^{124}I, as compared to OSEM. The dramatic dip seen in the ^{18}F MAP reconstruction in Figure 10 B may be interpreted as the contrast being far superior with MAP as compared to OSEM. This may be true to some extent, but the dip is most probably an artefact, of which an explanation is beyond the scope of this work. However, the presence of similar dips on both sides of the one in the middle may suggest that the artefact is caused by some kind of Fourier periodicity.

Comment on Corrections

The reason all reconstructions were done without applying any corrections for attenuation and/or Compton scatter was (a) the lack of equipment to accurately reproduce animal position, (b) mechanical problems with the transmission source mechanism, resulting in inconsistent and unreliable transmission scans, and (c) the lack of a point source that allowed transmission scanning of an animal containing positron emitting activity (i.e., at time points post injection). In order to allow such scans the transmission source has to be an emitter of gammas with energy clearly distinguishable from the primary and scattered annihilation photons. ^{57}Co (122 keV gammas) is commonly used for this purpose. Point (a) has to be considered since it is of prime importance that the emission data and the

corresponding transmission data match each other *(28)*. However, Fahey et al. concluded that attenuation correction may not be necessary for rodent imaging *(21)*. Considering the high energy of annihilation photons, attenuation is only likely to affect quantification in an object as small as a mouse in a minor way. Still, correction for attenuation may be worth implementing, provided it is done in a proper way.

As a direct consequence of the fact that transmission scans were not performed, scatter correction was not an option. This is because part of the input to the algorithm used by microPET Manager to correct for scattered events is a normalized attenuation corrected data set. One thing that could be worth a thought before using this kind of scatter correction with a non pure emitter, such as ^{124}I, is whether the scaling of the scatter profile involved in the algorithm in some way is affected by a background including a prompt gamma component. If this scaling (the procedure of which is not familiar to the author) is done based on the emission data it is possible that the difference in shape and level of the background, as compared to that of a pure emitter such as ^{18}F, may cause an over estimation of the scatter.

Animal Studies

Data for the mice used in the animal studies (injected activity, organ weights, quantified values etc.) can be found in Appendix A.

^{18}F-FDG Study

The outcome of the comparison of the quantification of ^{18}F activity concentration based on PET AVVs and the appropriate calibration factor as compared to the direct assay results (used as reference) is found in Figure 11.

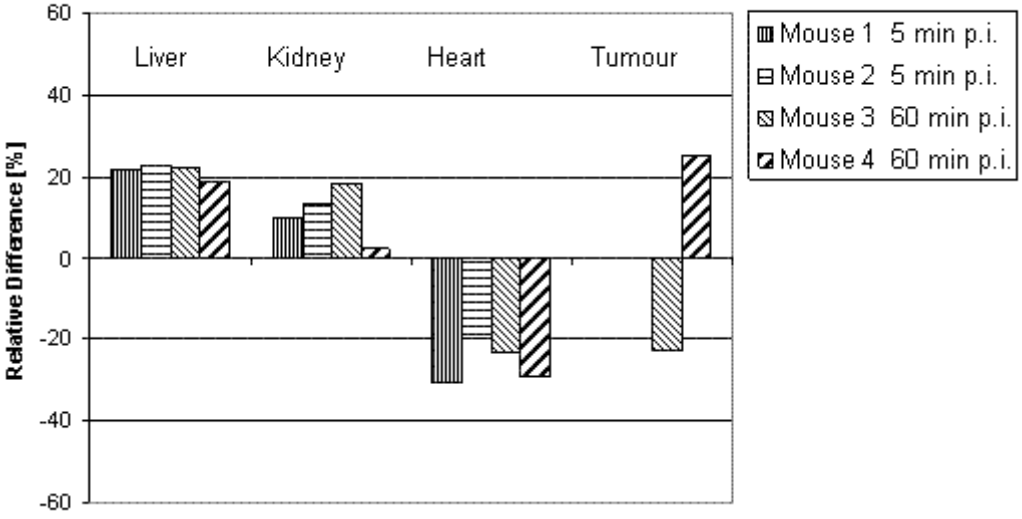

FIGURE 11. Differences in quantified ^{18}F-FDG activity concentrations using direct assay and PET image data. The difference is expressed as the PET result relative to the result of the direct assay.

The PET quantification underestimates (in the case of heart) and overestimates (in the cases of liver and kidneys) the activity concentration in normal organs of the same kind by roughly the same degree, and all deviations are within approximately ± 30 %. The overestimation in the case of the livers is probably due to a certain contribution from surrounding tissue and organs (possibly primarily from intestines). At the 5 minute time point contribution from hot blood within the liver, some of which is easily lost in the dissection process, may have an influence leading to an *ex vivo* direct assay value lower than the *in vivo* PET value. In the same way, loss of blood content may to some extent also be the cause of the overestimation of the kidney activity concentration. However, blood loss does not explain the underestimation of the heart activity concentration, the cause of which is not very clear. One factor that certainly affects the result here is the way in which the VOI is defined. A slightly smaller VOI in the case of heart may very well have given a result in good agreement with that of the direct assay. On the other hand, the VOIs used for kidney were defined in the same way as those for heart, and a reduction in the size of the kidney VOIs would have resulted in an even more pronounced overestimation. Clearly, VOIs defined in a similar way may give different variations when applied to different kinds of organs; overestimation for some and underestimation for others. Hence, biological as well as geometrical differences between different kinds of organs have to be considered. An assessment of this, and the differences seen between the *in vivo* and *ex vivo* results in general, is beyond the scope of this work. Nonetheless, it is

apparent that several factors, biological and physical as well as those having to do with experimental procedures, most certainly affect a comparison of this kind. This is something one has to keep in mind and be aware of when methods that rely on measurements acquired under different conditions are used, such as the normalization procedure in this work. One of the factors worth further investigation is the method of defining VOIs.

Unfortunately neither of the tumours in the mice scanned 5 minutes p.i. (mouse #1 and #2) were visualized in the PET images (the tumour in mouse #2 was negligibly small). Therefore, only two tumour results were obtained. These may be thought of as rather puzzling and ambiguous. Clearly, two results are too few to conclude anything about how the PET image quantification of small tumours differs from that of the direct assay. One may, however, consider the overestimation of the activity concentration in a (small) tumour, as in the case of mouse #4, as quite odd and unlikely. The tumours in mouse #3 and 4 were 3-4 mm in diameter, hence, with regard to the partial volume effect and the measured FWHM of just under 2 mm an underestimation of the activity concentration is what one would expect. The result of the quantification of the tumour in mouse #3 is in good compliance with this line of argument. One possible explanation of the overestimation of the activity concentration in the mouse #4 tumour may be that some small part of the tumour was left in the mouse when it was dissected, meaning that a lower activity was measured in the direct assay. Another, similar, possibility is that a small fraction of the tumour was lost in between the weighing and when it was put into the vial in which it was measured by the gamma counter.

^{124}I-cT84.66 Study

Figure 12 demonstrates the good agreement between the actual quantified blood samples and the PET data after normalization. The differences seen between the direct assay and PET values suggest that a reasonable estimation of the uncertainty in the quantified activity concentrations after normalization is within approximately ± 10% at the most, with the larger deviations in the early time-points. This good agreement shows that the PET image quantification is capable of accurately reproducing the change in activity concentration over time, hence the shape of the curve, and that the actual amplitude is effectively adjusted for by normalization to the direct assay result corresponding to the last time point.

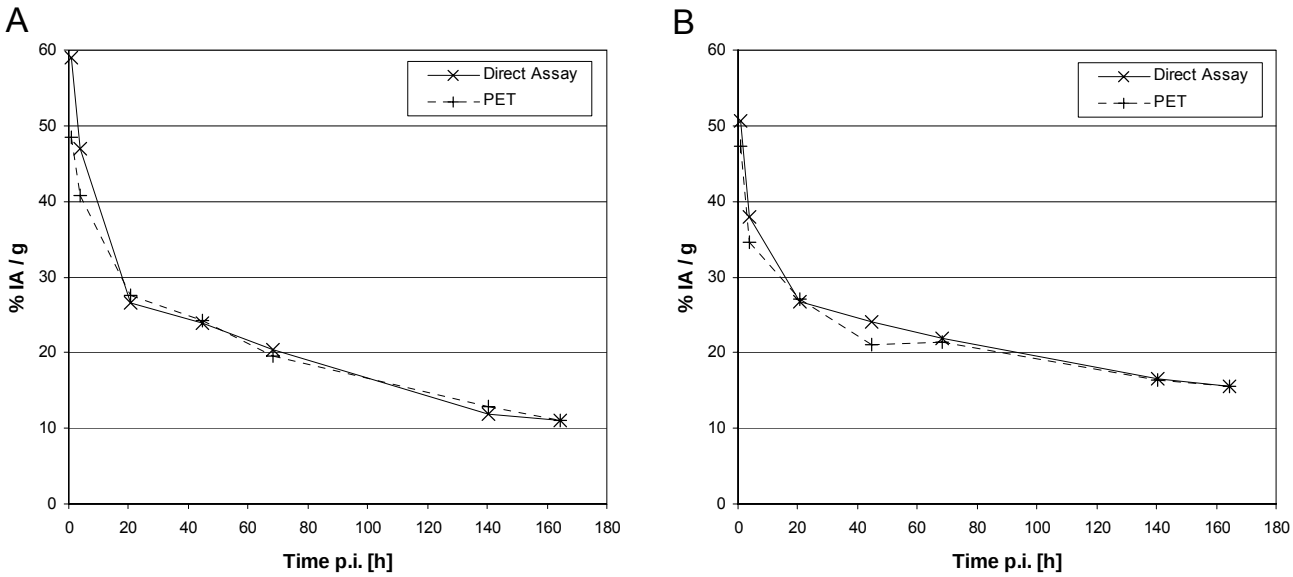

FIGURE 12. Quantified blood activity concentrations in mouse #1 (A) and mouse #2 (B). Compared are the results of the quantification based on direct assay of tail vein blood samples and that based on the PET data (normalized as described in the Materials and Methods section). The activity concentrations are expressed as percent injected activity per gram (% IA / g) and the data are corrected for physical decay.

Figure 13 shows how the antibody clears from the blood, liver and whole body and is effectively trapped in the tumour. The last data points in the two studied cases may seem to give an ambiguous suggestion whether or not the retention in the tumour is likely to continue to rise or start to decrease after 140 h p.i. There is off course a margin of error within which these data points can vary. This considered, and using the ± 10% uncertainty discussed in the context of the blood curve comparison as a crude estimate of the error, it is clear that the last data points in both A and B (Figure 13) may actually represent a change in activity concentration opposite of that indicated by the graph. One interpretation, probably not considered too dramatic, could be that the truth lies in-between the two results, meaning that the antibody retention in tumour at this stage can be considered to have reached a somewhat constant level. On the other hand, given the almost fivefold difference in mass between the tumour in mouse #1 and #2, it is not surprising that the resulting uptake characteristics differ at least to some extent.

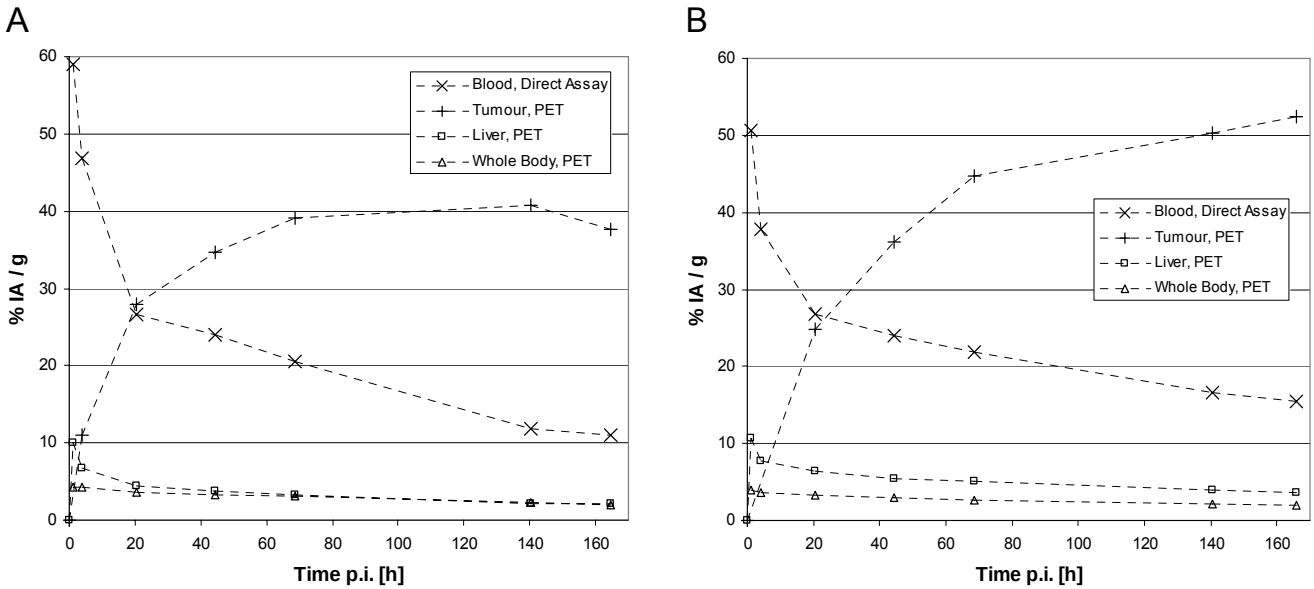

FIGURE 13. Decay corrected (pharmacokinetic) data for mouse #1 (A) and mouse #2 (B) demonstrating the uptake of the radio labelled antibody in tumour, in relation to the clearance from blood, liver and whole body. Activity concentration is here expressed in terms of percent injected activity per gram (% IA / g). PET data normalized as described in the Materials and Methods section.

Without going any further into the analysis of the curve shapes and what they might mean or imply in terms of pharmacokinetics, it should be pointed out that one thing is important to keep in mind when drawing conclusions from tracer data such as these. What the data represent is not (necessarily) the location and concentration of the actual molecule, but the tracer nuclide, in this case ^{124}I. The location of the tracer represents the distribution of interest only if the labelled molecule is intact under all conditions. Therefore, knowledge about the carrier molecule in terms of internalization and metabolism is of great importance and interest in this kind of pharmacokinetic studies. In this case, since the cT84.66 antibody is not internalized upon binding *(15)*, it is quite unlikely that the radiolabel would come loose and be transported away from the location of antibody uptake.

The values of the fit parameters obtained using ADAPT II are found in Table 4. Note that in the tumour case, one of the *A* coefficients had to be negative in order to fit the data increasing with time, i.e. the phase of uptake. Figure 14 shows the resulting fits, plotted together with the data points.

TABLE 4
Bi-Exponential Fit Parameter Values

Mouse #1

	A_1 (kBq/g)	A_2 (kBq/g)	k_1 (h^{-1})	k_2 (h^{-1})
Blood	613.1 ± 27.5	516.6 ± 24,7	0.1778 ± 0,0196	0.0126 ± 0,0009
Tumour	615.5 ± 50.7	-604.6 ± 49,8	0.0061 ± 0,0008	0.0839 ± 0,0150
Liver	124.7 ± 1.7	85.4 ± 1,1	0.3429 ± 0,0093	0.0124 ± 0,0003
Whole Body	8.3 ± 1.4	68.8 ± 1,5	0.1222 ± 0,0560	0.0108 ± 0,0005

Mouse #2

	A_1 (kBq/g)	A_2 (kBq/g)	k_1 (h^{-1})	k_2 (h^{-1})
Blood	473.1 ± 5.7	469.6 ± 3.7	0.2846 ± 0,0074	0.0108 ± 0,0002
Tumour	711.3 ± 83.7	-710.0 ± 83.7	0.0058 ± 0,0009	0.0441 ± 0,0066
Liver	98.7 ± 6.9	111.9 ± 3.5	0.4542 ± 0,0680	0.0111 ± 0,0006
Whole Body	10.3 ± 1.2	56.8 ± 0,7	0.3319 ± 0,0830	0.0830 ± 0,0002

A

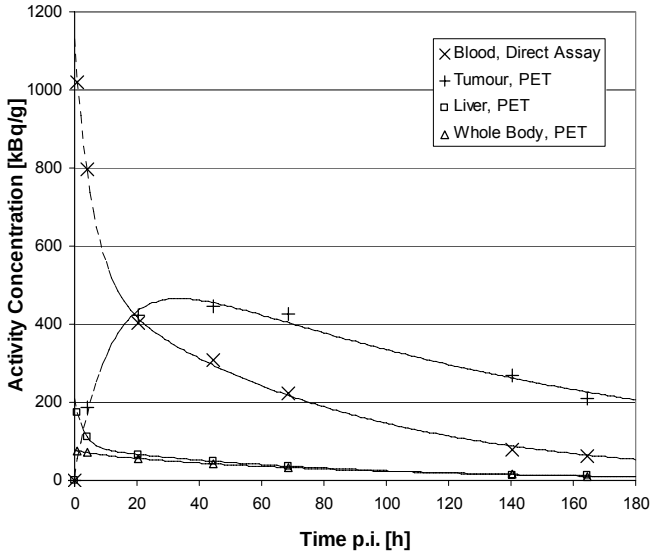

B

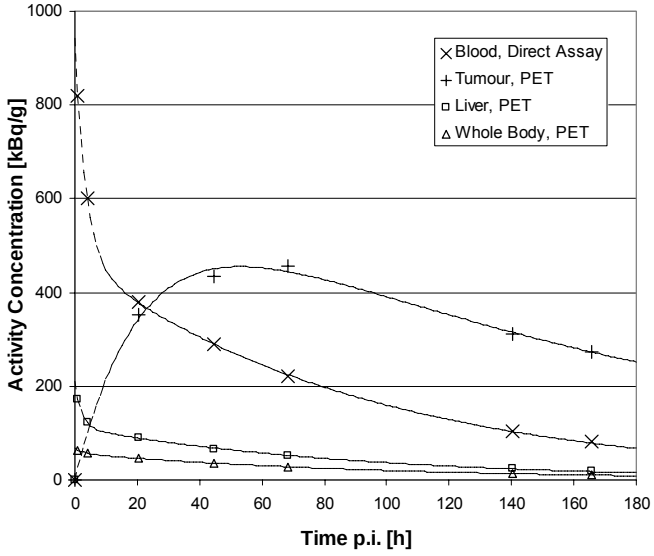

FIGURE 14. Non decay corrected time-activity data for mouse #1 (A) and mouse #2 (B) with the corresponding fits (dashed curves) of which the parameters can be found in Table 4. PET data normalized as described in the Materials and Methods section.

Integration of the fitted curves plotted in Figure 14 resulted in area-under-the-curve values (cumulated activities, $\tilde{A}$), which after division by the injected activity (per gram tissue) resulted in the residence times found in Table 5. Blood values are included for comparative reasons, although they were not used for any actual dosimetry within this work.

TABLE 5
Residence Time Values

	τ (h)	
	Mouse #1	Mouse #2
Blood	41.0 ± 3.3	49.3 ± 1.2
Tumour	10.2 ± 1.7	2.6 ± 0.6
Liver	5.7 ± 0.1	8.4 ± 0.5
Whole Body	84.8 ± 4.7	86.4 ± 2.6

The appreciable difference in residence time between the two tumours may at first seem surprising. However, it is simply explained by the large difference in tumour mass, resulting in a value about five times larger for the tumour in mouse #1 (the larger of the two tumours). The rest of the values seem to agree fairly well when the two mice are compared. The standard deviations found in Table 5 (calculated using the error propagation formula) are based on the errors listed in Table 4 and estimated errors in measurements of activity and organ weight.

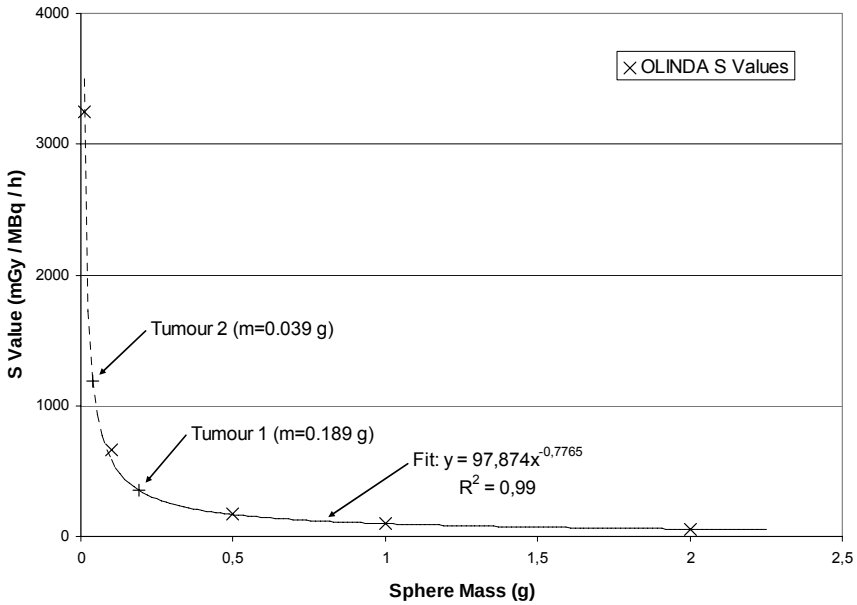

FIGURE 15. S values for five spheres of mass 0.01-2.00 g plotted along with a fitted power function (dashed) and the approximate S values for the tumours in mouse #1 and #2, given by the fitted function. The five sphere S values were obtained by using the sphere model included in the OLINDA software.

Figure 15 shows the data and fit from which the tumour S values were approximated. These, and the S values obtained by the digital mouse phantom Monte Carlo simulation are presented in Table 6. Found here are also the calculated mean absorbed doses, in terms of Gy per administered activity.

TABLE 6
S Values and Calculated Mean Absorbed Doses

	S (mGy MBq^{-1} h^{-1})	D/A_0 (Gy MBq^{-1})	
		Mouse #1	Mouse #2
Tumour 1 ← Tumour 1	355	3.62	-
Tumour 2 ← Tumour 2	1192	-	3.10
Liver ← Liver	35.4	0.20	0.30
Liver ← Whole Body	4.1	0.35	0.35
Whole Body ← Whole Body	3.6	0.31	0.31

Since tumour is not included in the digital mouse phantom the obtained S values omit any possible absorbed dose contributions from activity within the tumour. However, this most certainly has a minimal effect on the S values and calculated absorbed doses, since the absorbed dose contribution to the body itself from a tumour situated subcutaneously on the flank of a mouse to a good approximation can be considered negligible. Vice verse, the tumour S values and absorbed doses does not include any contribution from surrounding tissue and organs, since they are based only on the activity contained within a sphere.

It should also be mentioned that the tumour absorbed dose estimates done here do not take into consideration any change in tumour size during the experiment. Of course there was a certain growth of the tumours over the 8 days during which the mice were imaged, but the tumour were approximated with spheres of constant diameter based on the weight found in connection with the direct assay. Actual average tumour sizes smaller than those used in the calculations of the mean absorbed dose estimates would mean that the true mean absorbed doses could perhaps be higher than the estimates. Of course, this is a possibility only if the tumour growth at time points after those included in the study is negligible.

The calculated whole body absorbed dose may be used as a first approximation of the dose to the bone marrow *(29)*, which is the primary dose-limiting organ in radioimmunotherapy. The resulting estimated absorbed dose to the whole body of approximately 0.3 Gy can be compared to the radio toxicity level (LD_{50}) of 7 Gy for bone marrow in mice *(30)*. Although the administration of cT84.66 labelled with ^{124}I was intended primarily for imaging and not for therapy, it can be seen from the values in Table 6 that the therapeutic index (i.e., the ratio between mean absorbed dose in tumour and normal tissue) is in the order of 5 to 10. This indicates that ^{124}I provides not only imaging possibilities but also a certain therapeutic effect, not to be ignored. Combined with the constant progress in the field of antibody engineering, this will perhaps lead to an interest in a possible future use of ^{124}I for combined imaging and therapy in a clinical context.

General Conclusions & Future Work

This study indicates that the microPET R4 scanner is capable of reproducing changes in activity distribution of ^{124}I *in vivo*. By normalizing the relative uptake values from the PET images to a direct assay, done immediately after the last time point PET scan, quantification of activity concentration could be done under fairly straightforward conditions. This allowed absorbed dose estimates to be calculated.

It should be possible to use pharmacokinetic results based on quantitative imaging of ^{124}I, with time points distributed appropriately over a period of time (at least as long as the biological half-life of the studied molecule) for dose estimates when the molecule is labelled with radionuclides other than the imaging tracer (care has to be taken to the different physical half-lives, though). Of course, this is only true on condition that the pharmacokinetics are unaffected by a change of radionuclide. This should not be a problem as long as it is only a change of isotope of the element used for the quantitative study (e.g., going from imaging with ^{124}I to therapy using ^{131}I).

The reliability and accuracy of image based quantification greatly depends on the method of defining ROIs. This crucial step would be much helped by matching of the PET images to anatomical ditto, i.e., a CT data set. Therefore, it would be of great interest to perform an animal study, similar to the on presented here, including anatomical scanning using a small-animal CT scanner, providing matching and fusible functional (PET) and anatomical (CT) image data sets. An issue that has to be addressed in order to make such a multi-modality study useful is the need to be able to accurately reproduce animal position. Not only is this more or less a must in order to allow, and give meaning to, the image fusion. Reproducible positioning of the studied animal also allows the same set of ROIs to be used for all time points, a fact that should mean reduced uncertainty, as well as saved time.

When it comes to possible improvement of image quality and reduction of quantification uncertainty, it is apparent that there are quite a few areas of interest and potential. First of all, Monte Carlo simulations of ^{124}I in a digital rodent phantom would most likely give valuable understanding of what factors are those worth focusing on in order to improve microPET imaging with ^{124}I. Furthermore, thorough work could be put into optimization of reconstruction algorithm settings, and into studying the impact of implementing the different kinds of corrections, for example correction for attenuation, scatter and positron range. Also, scanner settings, such as the energy window's upper and lower threshold, could be optimized for improved performance with ^{124}I.

Acknowledgement

I would like to thank all the friendly and helpful people I have met during this study, among those in particular: My main supervisor **Prof. Sven-Erik Strand**, for introducing me to the field of radioimmunotherapy and for his guidance, as well as for many nice off-topic conversations; **Dr. Andrew Raubitschek** and **Dr. David Colcher**, for letting me work in their lab and for sharing interesting ideas, stories and thoughts; the **Raubitschek family**, for their tremendous hospitality; my on-site supervisors **Prof. Lawrence Williams** and **Dr. James Bading**, for introducing me to the field of small-animal imaging and their invaluable collaboration, help and advice; **Desiree Crow**, for all practical help with the mice and for being such a nice person in general; **Oliver Staak**, **Amit Ahuja** and **Michael Tempero**, for good company and nice chats at lunch in the (cold!) lab; **Prof. Magnus Dahlbom**, for discussions on, and explanations of, different questions related to PET, as well as for the enjoyable 4th July party; **Prof Michael Ljungberg**, for providing me with ^{124}I S values; **Enrique Cofresi**, for helping me out with work on my phantoms in the B.I.S. workshop; **Anders Örbom**, for good company in L.A.; and last, but not least, **Tibby** (R.I.P.), for keeping an eye on me, in the way only a good dog can.

REFERENCES

(1) Orlandi F, Caraci P, Mussa A, Saggiorato E, Pancani G, Angeli A. Treatment of medullary thyroid carcinoma: an update. *Endocr Relat Cancer*. 2001;(8):132-147.

(2) Hoefnagel CA. Nuclear medicine therapy of neuroblastoma. *Q J Nucl Med*. 1999;(43):336-343.

(3) Bodei L, Kassis AI, Adelstein SJ, Mariani G. Radionuclide Therapy with Iodine-125 and Other Auger-Electron-Emitting Radionuclides: Experimental Models and Clinical Applications. *Cancer Biotherapy and Radiopharmaceuticals*. 2003;18(6):861-877.

(4) Koppe MJ, Postema EJ, Aarts F, Oyen WJG, Bleichrodt RP, Boerman OC. Antibody-guided radiation therapy of cancer. *Cancer and Metastasis Reviews*. 2005;24(4):539-567.

(5) Lewis JS, Achilefu S, Garbow JR. Small animal imaging: current technology and perspectives for oncological imaging. *European Journal of Cancer*. 2002;38(16):2173-2189.

(6) Simon R.Cherry, Magnus Dahlbom. PET: Physics, Instrumentation and Scanners. In: Michael E.Phelps, ed. *PET Molecular Imaging and its Biological Applications*. Springer; 2004:1-124.

(7) Derenzo SE. Mathematical Removal of Positron Range Blurring in High-Resolution Tomography. *IEEE Trans Nucl Sci*. 1986;33:565-569.

(8) Hoffman EJ, Huang S-C, Phelps ME. Quantitation in positron emission computed tomography: I. Effect of object size. *J Comput Assist Tomogr*. 1979;3(3):299-308.

(9) Lee FT, Hall C, Rigopoulos A et al. Immuno-PET of human colon xenograft-bearing BALB/c nude mice using I-124-CDR-grafted humanized A33 monoclonal antibody. *J Nucl Med*. 2001;(42):764-769.

(10) Robinson MK, Doss M, Shaller C et al. Quantitative Immuno-Positron Emission Tomography Imaging of HER2-Positive Tumor Xenografts with an Iodine-124 Labeled Anti-HER2 Diabody. *Cancer Res*. 2005;65(4):1471-1478.

(11) Cherry SR, Shao Y, Silverman RW et al. MicroPET: a high resolution PET scanner for imaging small animals. *Nuclear Science, IEEE Transactions on*. 1997;44(3-part-2):1161-1166.

(12) Knoess C, Lenox M, Goble RN et al. Comparative study of ECAT HRRT and micropet R4 for animal PET studies. *Nuclear Science Symposium Conference Record, 2002 IEEE*. 2002;2:807-810.

(13) Knoess C, Siegel S, Smith A. Performance evaluation of the microPET R4 PET scanner for rodents. *European Journal of Nuclear Medicine & Molecular Imaging*. 2003;30(5):737-748.

(14) Sheh Y, Koziorowski J, Balatoni J, Lom C, Dahl JR, Finn RD. Low energy cyclotron production and chemical separation of "no carrier added" iodine-124 from a reusable,

enriched tellurium-124 dioxide/aluminum oxide solid solution target. *Radiochim Acta*. 2000;88:169-173.

(15) Neumaier M, Shively L, Chen FS et al. Cloning of the genes for T84.66, an antibody that has a high specificity and affinity for carcinoembryonic antigen, and expression of chimeric human/mouse T84.66 genes in myeloma and Chinese hamster ovary cells. *Cancer Res*. 1990;50(7):2128-2134.

(16) Millar WT, Smith JF. Protein iodination using Iodogen. *Int App Rad Isot*. 1983;34:639-641.

(17) Richardson AP, et al. An improved Iodogen method of labelling antibodies with I-123. *Nuclear Medicine Communications*. 1986;7:355-362.

(18) Hudson HM, Larkin RS. Accelerated image reconstruction using ordered subsets of projection data. *Medical Imaging, IEEE Transactions on*. 1994;13(4):601-609.

(19) Defrise M, Kinahan PE, Townsend DW, Michel C, Sibomana M, Newport DF. Exact and approximate rebinning algorithms for 3-D PET data. *Medical Imaging, IEEE Transactions on*. 1997;16(2):145-158.

(20) Ruangma A, Laforest R, Bing B, Leahy RM. Characterization of USC-MAP Image Reconstruction on MicroPET-R4. *Nuclear Science Symposium Conference Record, 2004 IEEE*. 2004;6:3449-3453.

(21) Fahey FH. Evaluation of the quantitative capability of a high-resolution positron emission tomography scanner for small animal imaging. *J Comput Assist Tomogr*. 2004;28(6):842-848.

(22) Bading JR, Yoo PB, Fissekis JD, Alauddin MM, D'Argenio DZ, Conti PS. Kinetic Modeling of 5-Fluorouracil Anabolism in Colorectal Adenocarcinoma: A Positron Emission Tomography Study in Rats. *Cancer Res*. 2003;63(13):3667-3674.

(23) Diehl KH, Hull R, Morton D et al. A good practice guide to the administration of substances and removal of blood, including routes and volumes. *Journal of Applied Toxicology*. 2001;21(1):15-23.

(24) Loevinger R, Budinger TF, Watson EE. *MIRD Primer for absorbed dose calculations*. New York, NY: The Society of Nuclear Medicine; 1991.

(25) D'Argenio DZ, Schumitzky A. A program package for simulation and parameter estimation in pharmacokinetic systems. *Comput Prog Biomed*. 1979;9:115-134.

(26) Segars WP, et al. Development of a 4D digital mouse phantom for molecular imaging research. *Molecular Imaging & Biology*. 2004;6(3):149-159.

(27) Stabin MG, Sparks RB, Crowe E. OLINDA/EXM: The Second-Generation Personal Computer Software for Internal Dose Assessment in Nuclear Medicine. *J Nucl Med*. 2005;46(6):1023-1027.

(28) Hoffman EJ, Huang S-C, Phelps ME, Kuhl DE. Quantitation in positron emission computed tomography: 2. Effects of inaccurate attenuation correction. *J Comput Assist Tomogr*. 1979;3(6):804-814.

(29) Wahl RL, Kroll S, Zasdny KR. Patient-specific whole body dosimetry: principles and a simplified method for clinical implementation. *J Nucl Med*. 1998;39(8 suppl):14S-20S.

(30) Hall EJ. *Radiobiology for the Radiologist*. Lippincott Williams & Wilkins; 2000:129-130.

^{18}F-FDG Study

Mouse #1

Injected Activity:	1354 kBq
Mouse Weight:	23 g

	Organ Weight (g)	Quantified Activity Concentration (kBq/g)	
		Direct Assay	PET
Liver	1.458	61.8	75.5
Kidneys	0.391	106.2	116.9
Heart	0.158	175.8	121.7
Tumour	0.005	207.6	n/v*

Mouse #2

Injected Activity:	1991 kBq
Mouse Weight:	24 g

	Organ Weight (g)	Quantified Activity Concentration (kBq/g)	
		Direct Assay	PET
Liver	1.294	97.7	119.9
Kidneys	0.313	173.9	197.6
Heart	0.169	330.8	264.6
Tumour	-	-	-

Mouse #3

Injected Activity:	2061 kBq
Mouse Weight:	25 g

	Organ Weight (g)	Quantified Activity Concentration (kBq/g)	
		Direct Assay	PET
Liver	1.319	27.4	33.7
Kidneys	0.381	173.9	205.7
Heart	0.147	373.7	286.0
Tumour	0.017	112.9	87.0

Mouse #4

Injected Activity:	2087 kBq
Mouse Weight:	22 g

	Organ Weight (g)	Quantified Activity Concentration (kBq/g)	
		Direct Assay	PET
Liver	1.111	52.9	62.9
Kidneys	0.315	102.1	104.3
Heart	0.128	1050.8	746.7
Tumour	0.028	135.8	169.8

* Not visualized in the PET images.

^{124}I-cT84.66 Study

Mouse #1

Injected Activity:	1743 kBq
Mouse Weight:	23 g

	Organ Weight** (g)
Blood	1.610
Liver	1.372
Tumour	0.189

	Quantified Activity Concentration (kBq/g)					
	Blood		Liver		Tumour	
Time Point (h p.i.)	Direct Assay	PET	Direct Assay	PET	Direct Assay	PET
1	1020.4	838.5	-	172.9	-	n/v*
4	795.2	691.2	-	112.9	-	187.5
21	402.7	418.0	-	66.3	-	422.6
45	307.1	311.2	-	49.5	-	445.2
69	222.7	212.9	-	36.3	-	424.8
141	78.3	85.8	-	14.3	-	270.2
165	62.3	62.3**	11.9	11.9***	211.3	211.3***

Mouse #2

Injected Activity:	1632 kBq
Mouse Weight:	25.5 g

	Organ Weight** (g)
Blood	1.785
Liver	1.324
Tumour	0.039

	Quantified Activity Concentration (kBq/g)					
	Blood		Liver		Tumour	
Time Point (h p.i.)	Direct Assay	PET	Direct Assay	PET	Direct Assay	PET
1	820.5	767.4	-	173.4	-	n/v*
4	601.1	584.3	-	123.1	-	n/v*
21	379.8	382.5	-	91.2	-	351.7
45	288.3	252.6	-	65.2	-	434.1
69	222.2	218.2	-	52.1	-	455.4
141	103.1	101.6	-	24.2	-	312.6
166	81.0	81.0**	19.2	19.2***	273.4	273.4***

* Not visualized in the PET images.
** At last time point, immediately after sacrifice.
*** Normalized to direct assay.